Brief Review

Modern Physics Letters B
Vol. 27, No. 29 (2013) 1330021 (13 pages)

DOI: 10.1142/S0217984913300214

World Scientific
www.worldscientific.com

RESISTIVE SWITCHING PHENOMENA IN COMPLEX OXIDE HETEROSTRUCTURES

YU-LING JIN, KUI-JUAN JIN*, CHEN GE, HUI-BIN LU and GUO-ZHEN YANG

Beijing National Laboratory for Condensed Matter Physics,
Institute of Physics, Chinese Academy of Sciences, Beijing 100190, China
**kjjin@iphy.ac.cn*

Received 8 October 2013
Accepted 9 October 2013
Published 23 October 2013

Resistive memories based on the resistive switching effect have promising application in the ultimate nonvolatile data memory field. This brief review focuses on the resistive switching phenomena in the perovskite oxide heterostructures, which originate from the modulation of the interface properties due to the movement of the oxygen vacancies and the ferroelectric polarization. Many recent experiments have been carried out to demonstrate the role of the oxygen vacancies by controlling the content of the oxygen vacancies in the oxide heterostructures with plenty of oxygen vacancies. The important role of the ferroelectric polarization was also carefully confirmed by analyzing the relationship between the *current–voltage* and *polarization–voltage* loops in the ferroelectric oxide heterostructures. The physical mechanisms have been revealed based on the developed numerical model.

Keywords: Resistive switching effect; perovskite oxide; oxygen vacancies; ferroelectric diodes; self-consistent calculation.

1. Introduction

The resistance switching random access memory (RRAM) is based on the resistive switching effect triggered by the applied electric field. The RRAM is a promising candidate for the next generation ultimate nonvolatile data memory with high density, great scalability and low power consumption.[1,2] Hickmott first reported the switchable resistance effect in the $Al/Al_2O_3/Al$ structure in 1962.[3] It is only applied in the special condition due to the limitation of the technology at that time.[4–6] With the development of memory technologies, the resistive switching effect has been found in various materials, such as binary oxides,[7–9] perovskite-type oxide,[10–12] and graphene.[13,14] Among these materials, the perovskite oxides are emerging as one of the leading materials due to their potential multifunctionality and the change ability of the nonstoichiometry of oxygen. In 2000, Liu *et al.* reported that the resistance of the $Pr_{0.7}Ca_{0.3}MnO_3$ thin film changed more than 1700%

under the electric pulse.[15] That promoted the study on the applications of the resistive switching effect in oxide films. At the same time, the multilevel switching was observed in the $SrZrO_3$ films by controlling the amplitude and length of the write pluses.[16] Recent outstanding investigations open up the broad possibility for the use of resistive switching effect in the market.[17–21]

In addition, the phenomena that two resistance states can be modulated by the electric field in the ferroelectric materials has also attracted much attention in the field of resistive switching. The memory based this effect is usually called as ferroelectric resistive random access memory (FeRRAM).[22,23] According to the conduction mechanisms, the ferroelectric resistive switching memories are divided into ferroelectric tunnel junctions and ferroelectric diodes.[24–28] In the case of ferroelectric tunnel junctions, the tunneling current plays the dominant role in transport of the ultrathin ferroelectric films. In the case of ferroelectric diode, the drift-diffusion or thermionic emission is the dominant process. This review article focuses on the latter case.

The RRAM and FeRRAM are generally built in the simple sandwich structures with the functional materials inserted between the top and bottom electrodes. The contact resistance between the electrodes and the perovskite oxide films can be changed by the applied voltage. So far, several models have been proposed to explain the mechanisms of the resistive switching effect by considering the effects of the interface, such as the modulation of the Schottky barrier, the charge trapping and discharging, and the oxidation/reduction reaction at the interface.[12,20,29–31] The migration of the oxygen vacancies at the interface is proposed to play an important role in the resistive switching effect. Many experimental and theoretical researches have been carried to investigate the role played by oxygen vacancies in the oxides.[32–34] The experimental results show that the resistive switching properties can be changed by controlling the experimental condition and oxidative treatment of the oxides.[35–40] Sawa reported the bipolar switching in the semiconducting oxides caused by the change of the Schottky barrier at the interface due to the migration of the oxygen vacancies.[12] The results showed that the device resistance is correlated with the area of the electrode. In addition, the work function and the oxygen affinity of the electrode can both affect the contact resistance at the interface.[12,41–44] Rozenber *et al.* presented a generic model to prove the movement of oxygen vacancies resulted in the resistive switching effect by Monte Carlo simulations.[45,46] The model, which combines the experimental evidence developed by Nian *et al.*, explained the resistive switching effect of $Pr_{0.7}Ca_{0.3}MnO_3$ by considering the movement of oxygen vacancies at the interface.[47]

In the metal-ferroelectric-metal (MFM) structure, many investigations found that the ferroelectric polarization played a dominant role in the switchable diode effect and the resistive switching effect.[48–51] To exclude influence of the migration of the oxygen vacancies, the oxygen vacancies in $BiFeO_3$ (BFO) layer were removed by applying a dc bias of +15 V on the sample for 30 min.[50] The results show that the

electrical hysteresis is connected with the ferroelectric polarization by measuring the *current–voltage* (I–V) and *polarization–voltage* (P–V) loops. Moreover, the switchable diode-like characteristics exhibited in the BFO films are governed by the switching of the ferroelectric domain, when the device is under the large electric field.

In this paper, we review our recent investigations in the resistive switching effect in the oxygen-deficient $LaMnO_3$ and the ferroelectric $BiFeO_3$ heterostructures. In the following section, we will discuss the experimental progress in the resistive switching of the perovskite oxide heterostructures. Then, the underlying physical mechanisms will be discussed in the viewpoint of theory based on the self-consistent calculations. Finally, the contents of the paper are summarized in Sec. 4.

2. Experiment Results

2.1. *Oxygen vacancies induced resistive switching effect in oxygen-deficient $LaMnO_3$ films*

To study the role played by oxygen vacancies in the resistive switching property, a comparative study was carried out in $LaMnO_3$ (LMO) films. Oxygen-deficient LMO films with different concentrations of oxygen vacancies were obtained by fabricating under various oxygen pressures. The LMO films were directly deposited on the $SrNb_{0.01}Ti_{0.99}O_3$ (SNTO) substrates by computer-controlled laser molecular beam epitaxy (LMBE) under the oxygen pressure of 10 Pa, 5×10^{-2} Pa and 5×10^{-4} Pa, respectively. The details of experiment can be found in Ref. 38. The c-axis lattice constant of LMO films becomes larger with the decrease of the oxygen pressure, which can be observed by synchrotron-based X-ray diffraction (SXRD). Moreover, sophisticated aberration-corrected scanning transmission electron microscopy (STEM) was utilized to further characterize the concentration of oxygen vacancies and structural evolution of LMO films. With the developments of aberration-corrected electron optics, the performance of microscope is enhanced to identify the individual light atoms. Thus, the aberration-corrected annular-bright-field (ABF) imaging technique is extremely sensitive to the presence of oxygen vacancies. Figures 1(a)–1(c) show the typical cross-section ABF micrographs of the LMO/SNTO junction viewed along the [001] axis. La, Mn and O sites can be distinguished according to the image contrast. La is represented as the darkest spots, whereas O is the lightest. The LMO film fabricated under lower oxygen pressure 5×10^{-4} Pa exhibits substantial structural distortions due to the extreme O depletion condition. That may lead to the formation of lattice defects as shown in Fig. 1(c). Line profiles along the vertical and horizontal directions with the markers in Figs. 1(a)–1(c) are shown in Figs. 1(d)–1(f) and 1(g)–1(i), respectively. The arrows in Figs. 1(d)–1(f) pointed the O site. The red/blue disks represent the stacking sequences of O-Mn. The lighter red disks stand for the presence of O vacancies. Results show that the concentration of oxygen vacancies in LMO film is increasing with the decrease of the oxygen pressure.

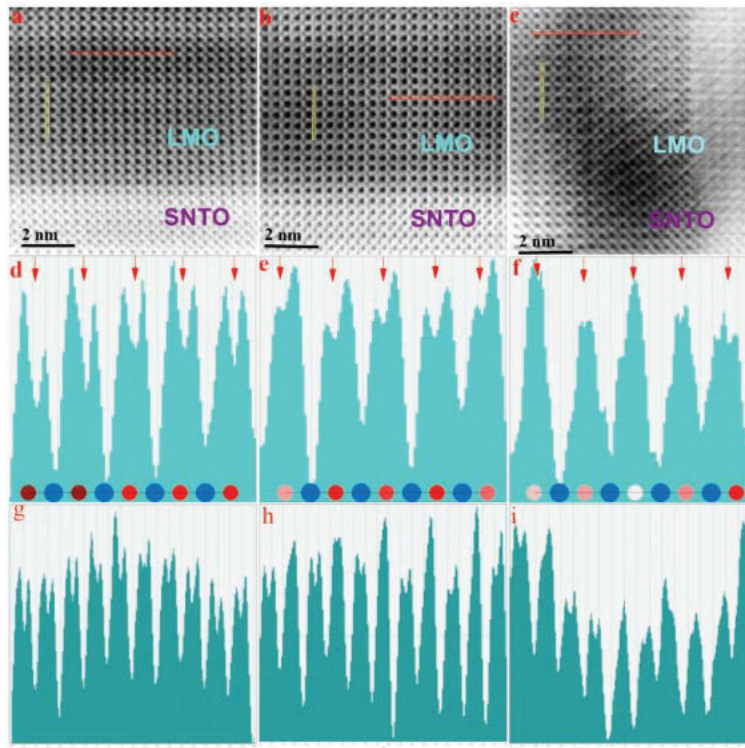

Fig. 1. (Color online) (a)–(c) ABF micrographs of the LMO/SNTO interfaces along the [001] axis in which the LMO films were fabricated under the oxygen pressures of 10 Pa, 5×10^{-2} Pa and 5×10^{-4} Pa, respectively. La is represented by the darkest spots, whereas the lightest represents O. (d)–(f) Line profiles along the vertical direction with respect to the markers are shown in (a)–(c). Red arrows point the O sites. The red/blue disks display stacking sequences of O-Mn; lighter red ones represent the presence of O vacancies. (g)–(i) Line profiles along the horizontal direction with respect to the markers are shown in (a)–(c). Reprinted (Fig. 2) with permission from *Small* **8** (2012) 1279.

The forward-bias is defined by the positive voltage applied on the top electrode (TE) Pt. Figure 2 shows the I–V curves of Pt/LMO/SNTO with obvious rectifying property and bipolar resistive switching behavior. The voltage bias applied on the TE Pt is in the direction of -1.5 V $\rightarrow$ 0 V $\rightarrow$ 3 V $\rightarrow$ 0 V $\rightarrow$ 1.5 V, which is indicated by the arrows in four branches as shown in Fig. 2. The resistance of Pt/LMO/SNTO is switched from the low resistance state (LRS) to the high resistance state (HRS) under the forward-bias. The results show that the switching hysteresis is more pronounced when the device is under forward-bias than that under reverse-bias. The resistive switching effect is suppressed with increasing the oxygen pressure. It indicates that the larger resistive switching can be obtained in the LMO film with higher concentration of oxygen vacancies in a certain range.

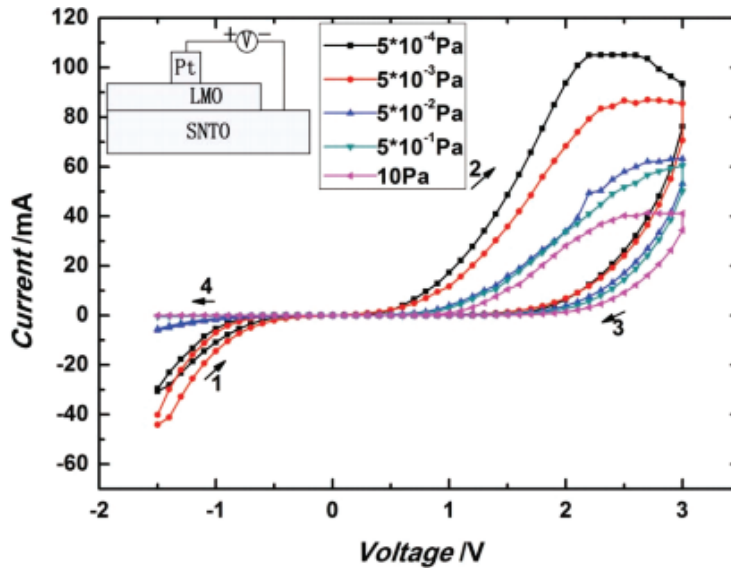

Fig. 2. (Color online) The I–V characteristics of Pt/LMO/SNTO in which the LMO films were fabricated under 10 Pa, 5×10^{-2} Pa and 5×10^{-4} Pa, respectively. Reprinted (Fig. 3) with permission from *Small* **8** (2012) 1279. ©2012 WILEY-VCH Verlag GmbH & Co. KGaA, Weinheim.

2.2. *The resistive switching in ferroelectric $BiFeO_3$ thin films*

The epitaxial BFO films were grown on the $SrRuO_3$ (SRO) covered $SrTiO_3$ (001) single crystal by pulsed laser deposition. The details of deposition method and condition can be found in Ref. 49. The I–V characteristics of 240 nm BFO thin films with Pt as the TE were shown in Fig. 3(a). The measurement was repeated 25 cycles by sweeping the bias voltage on the TE from 8 V to −7.5 V and back to 8 V. The results show that a large resistive switching exits in the BFO film. Moreover, two I–V segments, which are plotted in the inset of Fig. 3(a), shows an obvious switchable diode-like rectifying characteristics. The diode polarity can be switched at about ±6 V, which is close to the coercive voltage of the BFO film. It reported that the I–V curves measured on the 240 nm BFO film shows that the electrical hysteresis became more pronounced with the increase of the voltage range. Figure 3(b) shows the I–V characteristics in the semilogarithmic scales of the 240 and 120 BFO films. The 120 nm BFO film exhibit weaker resistive switching effect under the applied voltage range around ±3 V. The ratio of the resistance at HRS to the resistance at LRS is 103 at −3 V for 240 nm BFO film and it is 79 at −1 V for the 120 BFO film.

To investigate the influence of the film thickness on the resistive switching, the BFO film of 150, 300, 450 and 600 nm were grown on the $La_{0.7}Sr_{0.3}MnO_3$ (LSMO) covered the STO. The I–V characteristics of Au/BFO/LSMO/STO with various

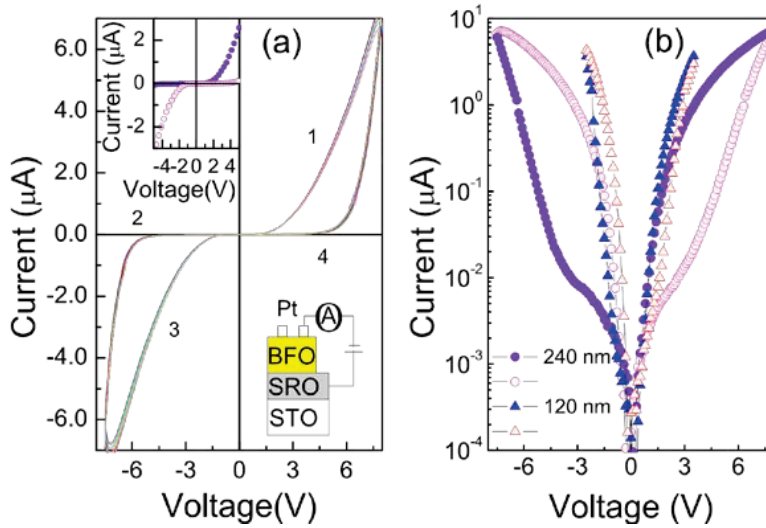

Fig. 3. (Color online) (a) The I–V curves measured on a 240 nm BFO film; Inset in the left is the I–V curves at the voltage range of ±5 V, which indicate the forward and reverse diode characteristics. The numbers denote the sequence of the voltage sweeps. (b) The I–V curves of the 240 nm and 120 nm BFO films plotted on semilogarithmic scales. Reprinted (Fig. 1) with permission from *Appl. Phys. Lett.* **98** (2011) 192901. © 2011 American Institute of Physics.

BFO film thicknesses are shown in Fig. 4. It can be seen that the hysteresis behavior become weaker with the decrease of the thickness of the BFO film. In Fig. 4(b) the R_{high} and R_{low} are the HRS and LRS of Au/BFO/LSMO/STO with 600 nm BFO. Figure 4(b) shows the I–V curves plotted on semilogarithmic scales, the value of $R_{\text{high}}/R_{\text{low}}$ decreases when the thickness of BFO film decreases.

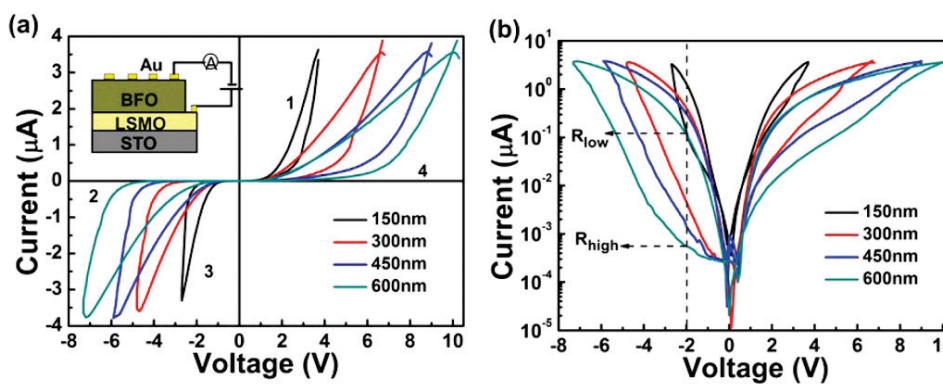

Fig. 4. (Color online) (a) The I–V curves of Au/BFO/LSMO/STO device with various BFO thicknesses. (b) The I–V curves are plotted on the semilogarithmic scales. The R_{high} and R_{low} are the HRS and LRS of Au/BFO/LSMO/STO with 600 nm BFO. Reprinted (Fig. 5) with permission from *Appl. Phys. Lett.* **102** (2013) 242902. © 2011 American Institute of Physics.

3. Theoretical Explanations

3.1. *The mechanism of the oxygen vacancies induced resistive switching*

As mentioned in the Introduction, it is found that the concentration of oxygen vacancies in the oxides could significantly affect the resistive switching effect. Because oxygen vacancies act as the mobile donors with positive charges after releasing the electron to the conduction band, the oxygen-deficient LMO films are considered as the n-type semiconductor. The formation of oxygen vacancies can be expressed using the Kröger–Vink notation as follows:

$$O_0 \leftrightharpoons \frac{1}{2}O_2 + V_0'' + 2e' \,. \tag{1}$$

The work function of Pt and SNTO are 5.3 eV and 4.05 eV, respectively.[52,53] The Schottky barrier would be formed at the interface of Pt and LMO, while the ohmic contact would appear at the LMO and SNTO. Thus, the obvious rectifying characteristics of the I–V loops are mainly caused by the Schottky junction, which is formed at Pt and LMO interface.

It is proposed that the change of the resistance of Pt/LMO/SNTO arises from modulating the Pt/LMO Schottky barrier by the movement of the oxygen vacancies under the applied electric field. When the device is under forward-bias, the positively charged oxygen vacancies will repelled away from the interface Au/LMO. Thus, the doping density at the vicinity of the Scottky junction would decrease. The height and width of the Schottky barrier became larger. The contact resistance, which contributes the major part of the whole resistance of the device, increases accordingly.

The properties of Pt/LMO Schottky junction can be obtained by self-consistently solving the Poisson and continuity equations as follows:

$$\frac{\partial^2\psi(x)}{\partial x^2} = -\frac{q}{\varepsilon}(p(x) - n(x) + N_d)\,, \tag{2}$$

$$\frac{\partial n(x)}{\partial t} = \frac{1}{q}\frac{\partial J_n(x)}{\partial x} - U(x)\,, \tag{3}$$

$$\frac{\partial p(x)}{\partial t} = -\frac{1}{q}\frac{\partial J_p(x)}{\partial x} - U(x)\,, \tag{4}$$

where $\psi(x)$, $n(x)$ and $p(x)$ are electrostatics potential, the concentration of electrons and holes, respectively. $J_n(x)$ and $J_p(x)$ are the current density of electrons and holes, respectively. $U(x)$ is the recombination rate of the Shockley–Read–Hall recombination process.[54,55] N_d, ε and q are doping density, the permittivity, and the electron charge. The concentration of electrons $n(x)$ and holes $p(x)$ are in relation with the quasi-Fermi potential of electrons $\phi_n(x)$ and holes $\phi_p(x)$ given by

$$n(x) = n_i \exp\left(\frac{q}{kT}(\psi(x) - \varphi_n(x))\right), \tag{5}$$

$$p(x) = n_i \exp\left(\frac{q}{kT}(\varphi_p(x) - \psi(x))\right). \tag{6}$$

The Richardson thermionic-emission-diffusion theory is adopted to build the boundary condition. The tunneling current is considered under the reverse-bias. The details of solving these equations can be found in Ref. 38.

Based on previous studies,[56–58] the impurity levels formed in the band gap due to the existence of the oxygen vacancies would narrow down the band gap width. With the increase of the concentration of oxygen vacancies, the number of free electrons increases and the electron mobility decreases because of the impurities scattering. The resistive switching effect is supposed to be resulted from the movement of the oxygen vacancies at the Schottky interface under the electric field. Thus, more oxygen vacancies in LMO films would lead to the larger variation of the Schottky barrier and result in the more pronounced resistive switching effect in a certain range. In the LMO film, which is fabricated under the 5×10^{-4} Pa, the concentration of the oxygen vacancies in the film is too high. Thus, the excessive structural distortions would be formed. The resistive switching effect of the LMO film fabricated under the 5×10^{-4} Pa does not improve more than that of the LMO film fabricated under the 5×10^{-3} Pa.

In the case of using Au as the TE, Schottky junction would also be formed at the interface of the Au and LMO. The Au/LMO/SNTO devices, in which LMO films were fabricated under 10 Pa, 5×10^{-2} Pa, 5×10^{-3} Pa and 5×10^{-4} Pa, respectively, have same resistive switching effect.[59] The calculated energy band diagrams of LMO films fabricated under the 5×10^{-3} Pa and 5×10^{-2} Pa are shown in Fig. 5. The variation of the Schottky barrier between LRS and HRS of the LMO films fabricated under the 5×10^{-3} Pa is larger than that of LMO film fabricated under 5×10^{-2} Pa, respectively.

3.2. *The mechanism of ferroelectric resistive switching and the switchable diode effect in BiFeO3 films*

In the MFM structure consisting of a thin BFO film, the Schottky junctions would be formed at the interface of the electrode and the BFO film. The resistive switching effect can be explained by the polarization-modulated Schottky-like barriers assumption.

In the Pt/BFO/SRO structure, the Schottky junctions would be formed at both top and bottom electrodes due to the work function of the Pt, n-type BFO and SRO are about 5.3 eV, 4.7 eV and 5.2 eV, respectively. A self-consistent model was proposed to explain the switchable diode effect by considering the incomplete screening effect in the MFM structure.[60,61] The fundamental charge transport equations are as follows:

$$\frac{d^2\varphi(x)}{dx^2} = -\frac{e}{\varepsilon(x)}\rho(x), \tag{7}$$

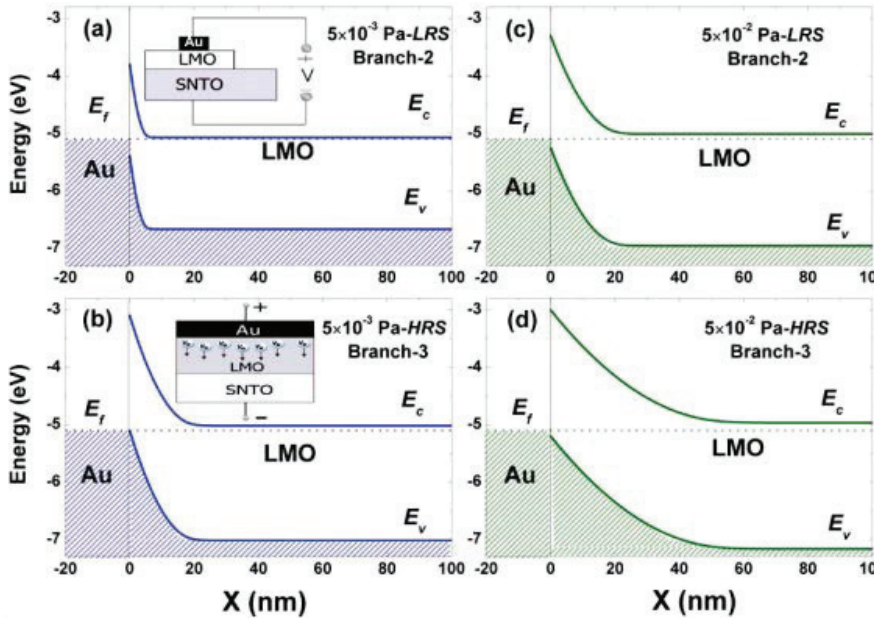

Fig. 5. (Color online) The energy band diagrams by calculating the Au/LMO Schottky junction at LRS and HRS, in which LMO films were fabricated under 5×10^{-3} Pa and 5×10^{-2} Pa. The inset of (a) and (b) are the measurement configuration and the schematic illustration of the movement of the oxygen vacancies. Reprinted (Fig. 3) with permission from *Mod. Phys. Lett. B* **27** (2013) 1350074. © 2013 World Scientific Publishing Co.

$$\frac{1}{e}\frac{dj(x)}{dx} - R(x) = 0\,, \tag{8}$$

$$j(x) = \frac{\sigma(x)}{e}\frac{d\kappa(x)}{dx}\,, \tag{9}$$

where e denotes the elementary charge. $\varphi(x)$, $\varepsilon(x)$, $\rho(x)$, $j(x)$, $R(x)$, $\sigma(x)$ and $\kappa(x)$ are the electrostatic potential, dielectric constant, charge density, current density, recombination rate, conductivity and electrochemical potential, respectively.

The polarization is treated as an infinite thin sheet of charges located at the interfaces for simplicity. Thus, the boundary condition can be expressed as

$$\varepsilon_s\varepsilon_0\frac{d\varphi(x)}{dx}\bigg|_{X_l^+} - \varepsilon_m\varepsilon_0\frac{d\varphi(x)}{dx}\bigg|_{X_l^-} = -\sigma(X_l) = P\,, \tag{10}$$

$$\varepsilon_m\varepsilon_0\frac{d\varphi(x)}{dx}\bigg|_{X_r^+} - \varepsilon_s\varepsilon_0\frac{d\varphi(x)}{dx}\bigg|_{X_r^-} = -\sigma(X_r) = -P\,, \tag{11}$$

where ε_0, ε_s and ε_m are the dielectric constant of vacuum, semiconductor and metal, respectively. σ, P and X_l, and X_r denote the interface charge density, the ferroelectric polarization, the position of left interface, and the position of right, respectively.

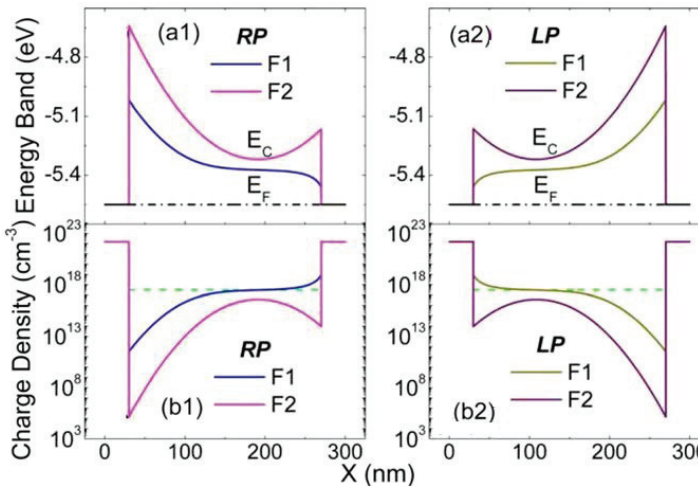

Fig. 6. (Color online) Band structures and charge density distributions under opposite ferroelectric polarizations. Reprinted (Fig. 2) with permission from *Appl. Phys. Lett.* **99** (2011) 063509. © 2011 American Institute of Physics.

In order to reveal the underlying mechanism behind the FeRRAM, the band diagrams and charge density distributions under opposite polarizations are obtained as shown in Fig. 6, in which the work function of ferroelectric materials F1 and F2 are 5.43 eV and 5.03 eV, respectively. The ferroelectric polarization P is assumed to be $\pm 30\ \mu C/cm^2$. Other parameters can be found in Ref. 60. If the direction of the polarization points to right shown in Fig. 6(a1), the negative polarization charges exists at the left interface, making the left interface barrier higher, while the positive polarization charges emerges at the right interface, making the left interface barrier lower. Then, if the polarization was reversed, the left interface barrier becomes lower, while the right interface barrier becomes higher as shown in Fig. 6(b1). Therefore, the barriers at the metal/ferroelectric interfaces can be modulated by the ferroelectric polarization under an enough high electric field. As a result, the polarity of the ferroelectric diode is switched with the polarization reversal. Thus, the switchable diode effect exists in the ferroelectric diodes. The resistive switching effect is attributed to the different barrier properties by changing the polarization direction. The resistance ratio of the Au/BFO/LSMO/STO is dependent on the thickness of BFO film. The value of R_{high}/R_{low} became larger with the increase of the thickness of BFO layer. It is proposed that the strain and the interfacial layer between BFO and LSMO play important roles in the electrical properties in the Au/BFO/LSMO/STO structure. Increasing the thickness of BFO film would result in decreasing the epitaxial strain and the substrate clamping, which may further increase the remnant polarization. The larger value of R_{high}/R_{low} in the Au/BFO/LSMO/STO structure with the thicker BFO film is due to the larger remnant polarization.

4. Conclusion

We have reviewed our recent progress of the resistive switching effect related with the properties of the interface of the complex oxides. The mechanisms for the nonferroelectric and ferroelectric resistive switching phenomena are clarified. The interface characteristics would be modulated due to the migration of the oxygen vacancies at the interface in the materials with enough oxygen vacancies. That would change the contact resistance which contributes the major part of the whole resistance of the device. A comparative study was carried out in oxygen-deficient LMO films with various concentrations of oxygen vacancies to demonstrate the role played by oxygen vacancies. The reverse of ferroelectric polarization can result in the switchable diode-like effect in the ferroelectric heterostructures. The different resistance states in the ferroelectric oxide heterostructure are related to the different directions of the polarization. The correlation between the local polarization and current versus applied voltage in BFO films was investigated to confirm the dominant role of ferroelectric polarization. In terms of theoretical investigations, the self-consistent numerical models are introduced to study the role of the oxygen vacancies and the polarization, respectively. The calculated band diagrams of the oxide heterostructures are employed to explain the role of the migration and concentration of the oxygen vacancies in the resistive switching effect. Another self-consistent model by considering the incomplete screening effect was proposed to explain the switchable diode effect in the MFM structure. The recent experimental and theoretical investigations may provide some foundations for the future progress of understanding the resistive switching effect. However, more efforts in both the experimental and theoretical aspects are still needed to develop toward the realization of the ultimate device application of the resistive memories.

Acknowledgments

This work was supported by the National Basic Research Program of China (Nos. 2012CB921403 and 2013CB328706) and the National Natural Science Foundation of China (Nos. 10825418 and 11134012).

References

1. R. Waser and M. Aono, *Nat. Mater.* **6** (2007) 833.
2. J. J. Yang, D. B. Strukov and D. R. Stewart, *Nat. Nanotechnol.* **8** (2012) 13.
3. T. Hickmott, *J. Appl. Phys.* **33** (1962) 2669.
4. G. Dearnaley, A. Stoneham and D. Morgan, *Rep. Prog. Phys.* **33** (1970) 1129.
5. D. Oxley, *Act. Passive Electron. Compon.* **3** (1977) 217.
6. H. Pagnia and N. Sotnik, *Phys. Status Solidi A* **108** (1988) 11.
7. J. J. Yang, M. D. Pickett, X. Li, D. A. Ohlberg, D. R. Stewart and R. S. Williams, *Nat. Nanotechnol.* **3** (2008) 429.
8. A. Chen, S. Haddad, Y. Wu, Z. Lan, T. Fang and S. Kaza, *Appl. Phys. Lett.* **91** (2007) 123517.

9. S. Seo, M. Lee, D. Seo, E. Jeoung, D.-S. Suh, Y. Joung, I. Yoo, I. Hwang, S. Kim and I. Byun, *Appl. Phys. Lett.* **85** (2004) 5655.
10. A. Asamitsu, Y. Tomioka, H. Kuwahara and Y. Tokura, *Nature* **388** (1997) 50.
11. E. Lee, M. Gwon, D.-W. Kim and H. Kim, *Appl. Phys. Lett.* **98** (2011) 132905.
12. A. Sawa, *Mater. Today* **11** (2008) 28.
13. F. Kreupl, R. Bruchhaus, P. Majewski, J. B. Philipp, R. Symanczyk, T. Happ, C. Arndt, M. Vogt, R. Zimmermann and A. Buerke, in *IEEE International Electron Devices Meeting*, San Francisco, 2008, pp. 1–4.
14. F. Zhuge, R.-W. Li, C. He, Z. Liu and X. Zhou, *Physics and Applications of Graphene — Experiments* (Intech, 2011), p. 421.
15. S. Liu, N. Wu and A. Ignatiev, *Appl. Phys. Lett.* **76** (2000) 2749.
16. A. Beck, J. Bednorz, C. Gerber, C. Rossel and D. Widmer, *Appl. Phys. Lett.* **77** (2000) 139.
17. D. S. Jeong, R. Thomas, H. Kohlstedt, A. Petraru and C. S. Hwang, *Rep. Prog. Phys.* **75** (2012) 076502.
18. A. K. Sharma, *Advanced Semiconductor Memories: Architectures, Designs, and Applications* (Wiley-IEEE Press, 2009).
19. R. Bruchhaus and R. Waser, Bipolar resistive switching in oxides for memory applications, *Thin Film Metal-Oxides* (Springer, 2010), p. 131.
20. R. Waser, R. Dittmann, G. Staikov and K. Szot, *Adv. Mater.* **21** (2009) 2632.
21. G. I. Meijer, *Science* **319** (2008) 1625.
22. J. F. Scott and C. A. Paz de Araujo, *Science* **246** (1989) 1400.
23. O. Auciello, J. F. Scott and R. Ramesh, *Phys. Today* **51** (1998) 22.
24. E. Y. Tsymbal and H. Kohlstedt, *Science* **313** (2006) 181.
25. M. Y. Zhuravlev, R. F. Sabirianov, S. Jaswal and E. Y. Tsymbal, *Phys. Rev. Lett.* **94** (2005) 246802.
26. V. Garcia, S. Fusil, K. Bouzehouane, S. Enouz-Vedrenne, N. D. Mathur, A. Barthelemy and M. Bibes, *Nature* **460** (2009) 81.
27. P. Maksymovych, S. Jesse, P. Yu, R. Ramesh, A. P. Baddorf and S. V. Kalinin, *Science* **324** (2009) 1421.
28. V. Garcia, M. Bibes, L. Bocher, S. Valencia, F. Kronast, A. Crassous, X. Moya, S. Enouz-Vedrenne, A. Gloter, D. Imhoff, C. Deranlot, N. D. Mathur, S. Fusil, K. Bouzehouane and A. Barthélémy, *Science* **327** (2010) 1106.
29. D. S. Jeong, H. Schroeder and R. Waser, *Phys. Rev. B* **79** (2009) 195317.
30. D. Shang, Q. Wang, L. Chen, R. Dong, X. Li and W. Zhang, *Phys. Rev. B* **73** (2006) 245427.
31. K. Tsubouchi, I. Ohkubo, H. Kumigashira, M. Oshima, Y. Matsumoto, K. Itaka, T. Ohnishi, M. Lippmaa and H. Koinuma, *Adv. Mater.* **19** (2007) 1711.
32. B. Bryant, C. Renner, Y. Tokunaga, Y. Tokura and G. Aeppli, *Nat. Commun.* **2** (2011) 212.
33. F. Nardi, S. Larentis, S. Balatti, D. Gilmer and D. Ielmini, *IEEE Trans. Electron Devices* **59** (2012) 2461.
34. S. Larentis, F. Nardi, S. Balatti, D. C. Gilmer and D. Ielmini, *IEEE Trans. Electron Devices* **59** (2012) 2468.
35. K. Shibuya, R. Dittmann, S. Mi and R. Waser, *Adv. Mater.* **22** (2010) 411.
36. S. Y. Wang, D. Y. Lee, T. Y. Huang, J. W. Wu and T. Y. Tseng, *Nanotechnology* **21** (2010) 495201.
37. L. Goux, P. Czarnecki, Y. Y. Chen, L. Pantisano, X. P. Wang, R. Degraeve, B. Govoreanu, M. Jurczak, D. J. Wouters and L. Altimime, *Appl. Phys. Lett.* **97** (2010) 243509.

38. Z. T. Xu, K. J. Jin, L. Gu, Y. L. Jin, C. Ge, C. Wang, H. Z. Guo, H. B. Lu, R. Q. Zhao and G. Z. Yang, *Small* **8** (2012) 1279.
39. J. P. Shi, Y. G. Zhao, H. J. Zhang, H. F. Tian and X. P. Zhang, *Appl. Phys. Lett.* **94** (2009) 192103.
40. P. Gao, Z. Kang, W. Fu, W. Wang, X. Bai and E. Wang, *J. Am. Chem. Soc.* **132** (2010) 4197.
41. T. Fujii, M. Kawasaki, A. Sawa, H. Akoh, Y. Kawazoe and Y. Tokura, *Appl. Phys. Lett.* **86** (2005) 012107.
42. T. Menke, P. Meuffels, R. Dittmann, K. Szot and R. Waser, *J. Appl. Phys.* **105** (2009) 066104.
43. T. Fujii, M. Kawasaki, A. Sawa, Y. Kawazoe, H. Akoh and Y. Tokura, *Phys. Rev. B* **75** (2007).
44. C. Dong, D. Shang, L. Shi, J. Sun, B. Shen, F. Zhuge, R. Li and W. Chen, *Appl. Phys. Lett.* **98** (2011) 072107.
45. M. Quintero, P. Levy, A. G. Leyva and M. J. Rozenberg, *Phys. Rev. Lett.* **98** (2007) 116601.
46. M. Rozenberg, I. Inoue and M. Sanchez, *Phys. Rev. Lett.* **92** (2004) 178302.
47. Y. B. Nian, J. Strozier, N. J. Wu, X. Chen and A. Ignatiev, *Phys. Rev. Lett.* **98** (2007) 146403.
48. A. Q. Jiang, C. Wang, K. J. Jin, X. B. Liu, J. F. Scott, C. S. Hwang, T. A. Tang, H. B. Lu and G. Z. Yang, *Adv. Mater.* **23** (2011) 1277.
49. C. Wang, K.-J. Jin, Z.-T. Xu, L. Wang, C. Ge, H.-B. Lu, H.-Z. Guo, M. He and G.-Z. Yang, *Appl. Phys. Lett.* **98** (2011) 192901.
50. D. Lee, S. Baek, T. Kim, J.-G. Yoon, C. Folkman, C. Eom and T. Noh, *Phys. Rev. B* **84** (2011) 125305.
51. S. Hong, T. Choi, J. H. Jeon, Y. Kim, H. Lee, H. Y. Joo, I. Hwang, J. S. Kim, S. O. Kang, S. V. Kalinin and B. H. Park, *Adv. Mater.* **25** (2013) 2339.
52. S. M. Sze, *Semiconductor Devices: Physics and Technology* (John Wiley & Sons, 2008).
53. P. Han, K.-J. Jin, H.-B. Lu, Q.-L. Zhou, Y.-L. Zhou and G.-Z. Yang, *Appl. Phys. Lett.* **91** (2007) 182102.
54. P. Han, K. J. Jin, Y. L. Zhou, X. Wang, Z. S. Ma, S. F. Ren, A. G. Mal'shukov and K. A. Chao, *J. Appl. Phys.* **99** (2006) 074504.
55. K. Yang, J. R. East and G. I. Haddad, *IEEE Trans. Electron Devices* **41** (1994) 138.
56. S. Picozzi, C. Ma, Z. Yang, R. Bertacco, M. Cantoni, A. Cattoni, D. Petti, S. Brivio and F. Ciccacci, *Phys. Rev. B* **75** (2007) 094418.
57. M. L. Wilson, J. M. Byers, P. C. Dorsey, J. S. Horwitz, D. B. Chrisey and M. S. Osofsky, *J. Appl. Phys.* **81** (1997) 4971.
58. R. Mahesh and M. Itoh, *Solid State Ion.* **108** (1998) 201.
59. Y.-L. Jin, Z.-T. Xu, K.-J. Jin, C. Ge, H.-B. Lu and G.-Z. Yang, *Mod. Phys. Lett. B* **27** (2013) 1350074.
60. C. Ge, K.-J. Jin, C. Wang, H.-B. Lu, C. Wang and G.-Z. Yang, *Appl. Phys. Lett.* **99** (2011) 063509.
61. C. Ge, K.-J. Jin, C. Wang, H.-B. Lu, C. Wang and G.-Z. Yang, *J. Appl. Phys.* **111** (2012) 054104.